mater.scichina.com link.springer.com

Published online 15 May 2020 | https://doi.org/10.1007/s40843-020-1328-y
Sci China Mater 2020, 63(9): 1672–1682

Metal-organic framework-derived Ni_2P/nitrogen-doped carbon porous spheres for enhanced lithium storage

Shi Tao[1†], Peixin Cui[2†], Shan Cong[1], Shuangming Chen[3], Dajun Wu[1], Bin Qian[1*], Li Song[3*] and Augusto Marcelli[4]

ABSTRACT **Transition metal phosphides (TMPs)/carbonaceous matrices have gradually attracted attention in the field of energy storage. In this study, we presented nickel phosphide (Ni_2P) nanoparticles anchored to nitrogen-doped carbon porous spheres (Ni_2P/NC) by using metal-organic framework-Ni as the template. The comprehensive encapsulation architecture provides closer contact among the Ni_2P nanoparticles and greatly improves the structural integrity as well as the electronic conductivity, resulting in excellent lithium storage performance. The reversible specific capacity of 286.4 mA h g^{-1} has been obtained even at a high current density of 3.0 A g^{-1} and 450.4 mA h g^{-1} is obtained after 800 cycles at 0.5 A g^{-1}. Furthermore, full batteries based on $LiNi_{1/3}Co_{1/3}Mn_{1/3}O_2$||$Ni_2P$/NC exhibit both good rate capability and cycling life. This study provides a powerful and in-depth insight on new advanced electrodes in high-performance energy storage devices.**

Keywords: nickel phosphide, metal-organic frameworks, X-ray absorption spectroscopy, pseudocapacitance behavior, lithium-ion batteries

INTRODUCTION

Current commercial lithium-ion batteries (LIBs) have dominated the marketplace for energy storage devices due to their high capacities, long span life and good rate capability [1–5]. However, the limited theoretical capacity of graphite anode is not sufficient to meet the demands of next generation of portable devices, electronic vehicles and electrical grids. Thus, searching for novel electrodes with higher energy and power density is more significant and urgent. To date, transition metal oxides, sulfides and phosphides have been widely reported as anode materials in high-performance rechargeable batteries [6–13]. Nickel phosphides, as important members of transition metal phosphides (TMPs), have been extensively studied in water splitting, lithium/sodium-ion batteries and electrochemical capacitors (ECs) [14–21]. However, large volume expansion and poor kinetic problems lead to the pulverization of electrode materials and inferior rate performance. Nanostructural Ni_2P, such as hollow spheres, nanowires and nanoparticles, have been reported to address the issue [22–24], but results are not effective, because the active material aggregated during the cycling. Therefore, it is urgent to design a carbon-coating and nickel phosphides framework to significantly enhance the electrochemical performances.

Since metal-organic frameworks (MOFs) made by multifunctional organic ligands and metal ions, have been extensively employed as soft templates to prepare carbon-encapsulated electrode materials for electrochemical energy storage applications [25–30]. Herein, we prepared the Ni_2P nanoparticles within nitrogen-doped carbon (Ni_2P/NC) porous spheres by using MOF-Ni templates and evaluated them as anodes for LIBs. Benifiting from the porous micro/nano-structure with a strong carbon skeleton, the as-prepared Ni_2P/NC exhibits both high structural stability and superior rate capability. Moreover,

[1] School of Electronic and Information Engineering, Jiangsu Laboratory of Advanced Functional Materials, Changshu Institute of Technology, Changshu 215500, China
[2] Key Laboratory of Soil Environment and Pollution Remediation Institute of Soil Science, Chinese Academy of Sciences, Nanjing 210008, China
[3] National Synchrotron Radiation Laboratory, University of Science and Technology of China, Hefei 230029, China
[4] INFN-Laboratori Nazionali di Frascati, Via E. Fermi 40, Frascati 00044, Italy
[†] These authors contributed equally to this paper.
[*] Corresponding authors (emails: njqb@cslg.edu.cn (Qian B); song2012@ustc.edu.cn (Song L))

X-ray absorption fine structure (XAFS) spectroscopy has been applied to investigate the change of local structure during the charge/discharge process. Full batteries are also assembled and demonstrate a good rate capability. This design can effectively improve the electronic conductivity and release the volume expansion during the electrochemical process.

EXPERIMENTAL SECTION

Synthesis of MOF-Ni spheres

The MOF-Ni spheres were synthesized by a solvothermal method. Briefly, 1 mmol of $Ni(NO_3)_2·6H_2O$ was dissolved in 30 mL of *N*,*N*-dimethylformamide (DMF) and ethylene glycol (EG) mixed solvent (2:1 in volume). Then, 1 mmol of *p*-phthalic acid was added to the solution, and stirred for 1 h. After that, the solution was transferred to a 50-mL teflon-sealed autoclave and maintained at 150°C for 6 h. The precipitates were centrifuged and washed with deionized water and methanol for several times, and then dried under vacuum at 80°C overnight to obtain the MOF-Ni spheres.

Synthesis of Ni_2P/NC porous spheres

The Ni_2P/NC porous spheres were fabricated *via* a low temperature phosphidation of MOF-Ni spheres. The as-prepared MOF-Ni and NaH_2PO_2 were placed at two separate positions in a corundum boat, with NaH_2PO_2 at the upstream side of the furnace. The molar ratio of the MOF-Ni to NaH_2PO_2 was 1:5. Then, the samples were heated up to 350°C for 2 h with a heating rate of 2°C min^{-1} in N_2 atmosphere. Finally, the black powder was obtained after the furnace was cooled down to ambient temperature.

Material characterization

The crystalline phase was recorded using the Bruker D8 ADVANCE with the Cu Kα radiation (λ = 0.15406 nm) at a scanning rate of 4° min^{-1}. Scanning electron microscopy (SEM) images of the products were obtained using the ZEISS microscope with an accelerating voltage of 20 kV. Transmission electron microscopy (TEM) images were obtained by a JEOL JEM-2000CX instrument. The X-ray photoelectron spectroscopy (XPS) was carried out with the PHI-5400 electron spectrometer. The Raman spectrum was performed on a Horiba Xplora with 532 nm laser excitation. The thermogravimetric analysis (TGA) was conducted from room temperature up to 1000°C with a heating rate of 5°C min^{-1} under flowing air (TGA, SDTA851). Ni K-edge XAFS spectra of all samples were recorded at the 1W1B beamline of Beijing synchrotron radiation facility.

Electrochemical measurements

The electrode was prepared by mixing 70 wt% Ni_2P/NC, 20 wt% acetylene black, and 10 wt% polyvinylidene difluoride (PVDF) in *N*-methylpyrrolidinone. The slurry was pasted onto Cu foil, and then dried at 110°C overnight under vacuum. The loading density of the active materials was about 1.8 mg cm^{-2} and the thickness of the electrode was 120 μm. CR2016-type coin cells were assembled in an argon-filled glovebox. Li-metal foil was used as the counter electrode and 1.0 mol L^{-1} $LiPF_6$ dissolved in ethylene carbonate (EC)/dimethl carbonat (DMC)/diethyl carbonate (DEC) (1:1:1 by volume) was used as the electrolyte. The charge-discharge tests were carried out on LAND CT2001A systems. The cyclic voltammetry (CV) curves were tested on a VSP electrochemical workstation (Bio-logic, France). To assemble the coin full cell, the Ni_2P/NC and $LiNi_{1/3}Co_{1/3}Mn_{1/3}O_2$ electrodes were used as the anode and the cathode, respectively. The $LiNi_{1/3}Co_{1/3}Mn_{1/3}O_2$ was purchased from Henan Cologne Group Co. (China), and the capacity ratio of the two electrodes was 1.2 (cathode/anode). The Ni_2P/NC electrode was pre-lithiated by directly contacting with lithium foil, and soaked into the electrolyte solution for 6 h. The full cells based on Ni_2P/NC|| $LiNi_{1/3}Co_{1/3}Mn_{1/3}O_2$ were charged and discharged over the voltage ranging from 0.5 to 3.5 V.

RESULTS AND DISCUSSION

Scheme 1 shows the preparation of Ni_2P/NC porous spheres. First, uniform MOF-Ni spheres were prepared by a facile solvothermal method. And then, the Ni_2P/NC composite was synthesized by using a low-temperature phosphidation process, converting MOF-Ni into Ni_2P/NC. After phosphating treatment, the Ni^{2+} ions can be transformed into Ni_2P nanoparticles and the MOF organic ligands are turned into the carbon frameworks.

MOF-Ni spheres exhibit a regular shape with some agglomeration as shown in Fig. 1a (also seen in Fig. S1). The Ni_2P/NC spheres can be clearly observed in Fig. 1b, c, with the shape well consistent with that of MOF-Ni. The rough surface results from the pyrolysis of the organic ligands during the phosphating treatment. The TEM images of the Ni_2P/NC (Fig. 1d, e and Fig. S2) show the uniform porous spheres, which consist of small Ni_2P particles assembled inside the N-doped carbon frameworks, with the diameter of 1–2 um. Fig. 1f, g show the HRTEM images of the Ni_2P nanoparticles observed at the

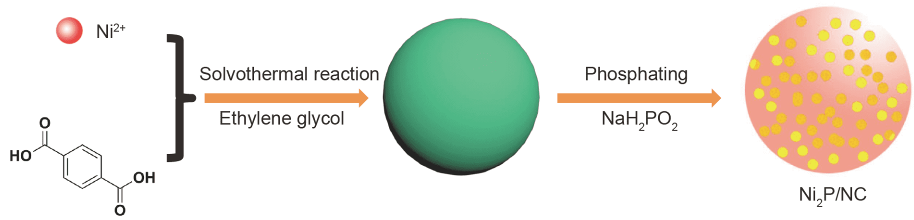

Scheme 1 Schematic illustration of the synthesis of Ni_2P/NC porous spheres.

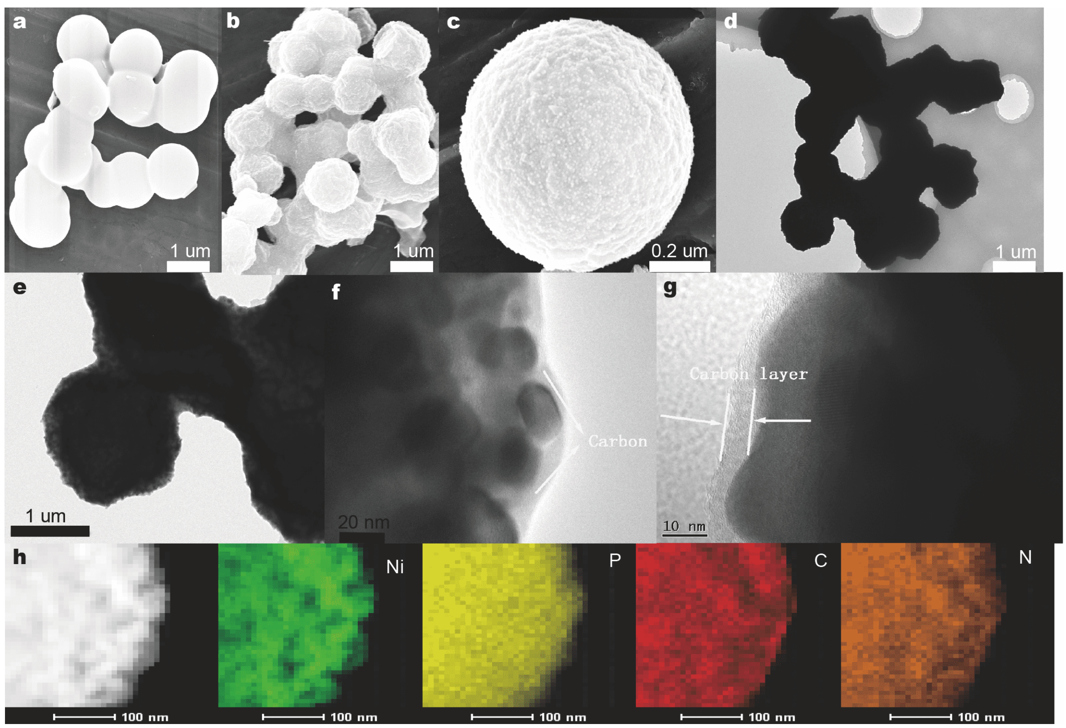

Figure 1 The morphology and microstructure of the as-prepared samples: (a) SEM images of the MOF-Ni; (b, c) the Ni_2P/NC with different magnifications; (d–f) TEM images of the Ni_2P/NC; (g) HRTEM image of the Ni_2P/NC; (h) elemental mapping of the Ni_2P/NC.

edge and surrounded by a N-doped carbon shell ~4 nm thick, which tightly confines each Ni_2P nanoparticle. Moreover, Fig. 1h presents the energy dispersive spectroscopy (EDS) maps with the uniform distribution of Ni, P, C and N elements in the Ni_2P/NC composite.

As shown in Fig. 2a, all the diffraction peaks match well with the standard Ni_2P (JCPDS No. 65-3544). No other phases were detected, indicating the purity of Ni_2P/NC. Fig. 2b shows the Raman spectra where the peaks at around 1342 and 1591 cm^{-1} are the characteristic D and G bands of carbon. The ratio of I_D/I_G=0.92 demonstrates the presence of high graphic carbon and good electronic conductivity [31–33]. The composition of Ni_2P/NC was determined by TGA in the O_2 atmosphere (Fig. 2c), in which the main loss occurs in the temperature range of 400 to 600°C attributed to the oxidation of carbon and Ni_2P decomposition. Then the residue begins to oxidize over 600°C and converts to stable $Ni_3(PO_4)_2$, $Ni_2P_2O_7$ and NiO (Fig. S3), leading to the increase of weight. Based on this analysis, the Ni_2P content can be calculated to be 66.7%. Fig. 2d provides the N_2 adsorption-desorption isotherm, resulting in a Brunauer-Emmett-Teller (BET) surface area of 34.5 m^2 g^{-1}. The pore size distribution curve exhibits about 10.5 nm mesopores in the Ni_2P/NC, which contributes to the electrode infiltrating in electrolyte and fasten the Li^+ diffusion [34].

As shown in Fig. S4, the Ni, P, C and N elements are clearly detected, in agreement with the EDS results in

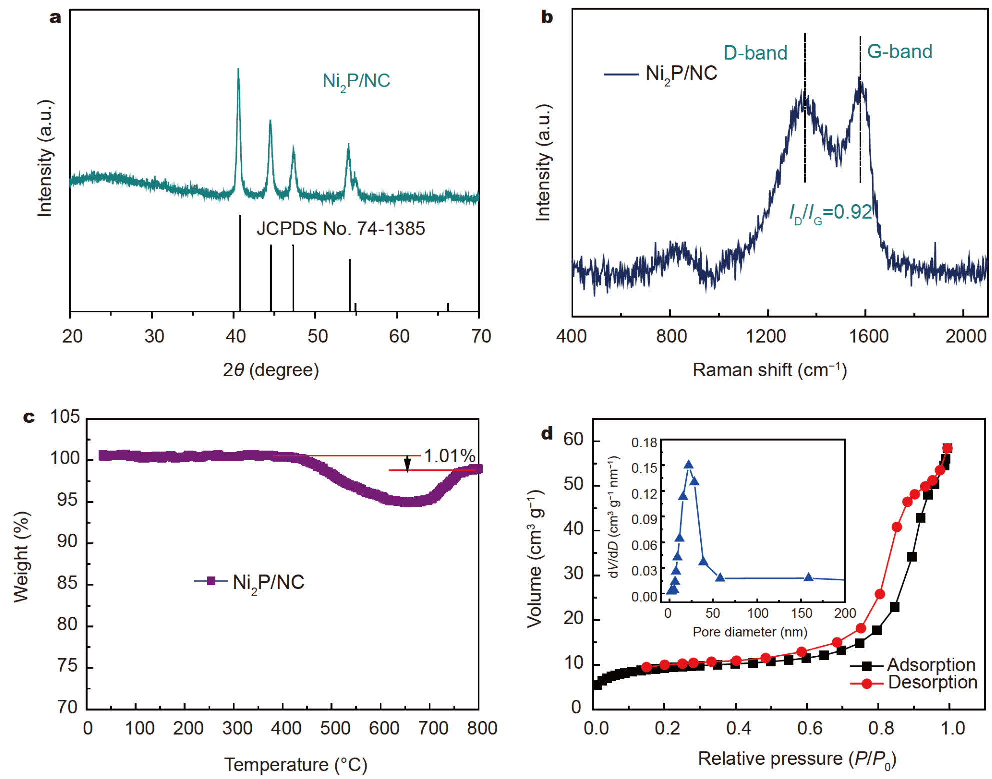

Figure 2 (a) XRD pattern , (b) the Raman spectra , (c) the TGA curves , and (d) the N_2 adsorption-desorption isotherms and pore size distribution (inset) of the Ni_2P/NC.

Fig. 2h. The N content in the composite can be determined to be 6.82% by the survey spectrum. The high-resolution XPS was also performed to investigate the chemical states (Fig. 3). The Ni 2p spectrum can be fitted into 6 peaks, and the Ni $2p_{3/2}$ and Ni $2p_{1/2}$ are located at 853.1 and 875.0 eV, respectively. In the spectrum of Ni_2P/NC, the area as well as the intensity suggests the Ni element mainly presents as Ni–P bonds [19,35]. In P 2p spectrum, the peak located at 129.9 eV corresponds to the P–Ni bonds in Ni_2P, while the peak at 134.7 eV is attributed to the oxidized P species, due to the exposure in air [36]. The spectrum of C 1s reveals three peaks, attributed to C–C (284.8 eV), C–N (285.6 eV) and C=O/C=C (286.8 eV), suggesting the carbon was N-doped [37]. Additionally, the high-resolution N 1s spectrum indicates the presence of pyridinic-N (399.7 eV), pyrrolic-N (400.3 eV), and graphitic-N (402.2 eV) [29,38].

The performance of battery with the Ni_2P/NC composite as anode materials is presented in Fig. 4. CV curves of the initial five cycles were obtained at 0.2 mV s^{-1} (Fig. 4a). The peak at 0.6 V is corresponding to the insertion of Li^+-ions into the Ni_2P, which forms the solid electrolyte interface (SEI) film in the first cycle [39,40]. Subsequently, the peak at 1.02 V in the anodic scan is associated to the decomposition of the SEI film and Li_3P [14,41]. In the following cycles, the main cathodic peak shifts to 1.6 V, corresponding to the structural change of Ni_2P into Li_3P and metal Ni [42,43]. Obviously, the subsequent CV curves exhibit good overlap, suggesting the superior reversibility of the Ni_2P/NC electrode. Fig. 4b shows that the charge-discharge profiles at a current density of 0.1 A g^{-1}. The first discharge/charge specific capacities are 1240.5/649.8 mA h g^{-1}, respectively. The high irreversibility of the capacities between the first charge and discharge cycles can be attributed to the formation of SEI film on the electrode surface, in good agreement with the CV behavior. The rate capability was tested at different current densities from 0.1 to 3.0 A g^{-1} (Fig. 4c, d), delivering the average discharge capacity of 587.8, 503.6, 437.3, 370.8, 342.6 and 286.4 mA h g^{-1} at 0.2, 0.5, 0.8, 1.0, 2.0 and 3.0 A g^{-1}, respectively. Notably, the discharge capacity recovered to 633.8 mA h g^{-1} after the deep cycling, suggesting a fast capacity response of Ni_2P/NC. Moreover, Fig. 4e presents the durability test. In particular, after 800 continuous charge-discharge cycles at the current density of 0.5 A g^{-1}, a reversible specific ca-

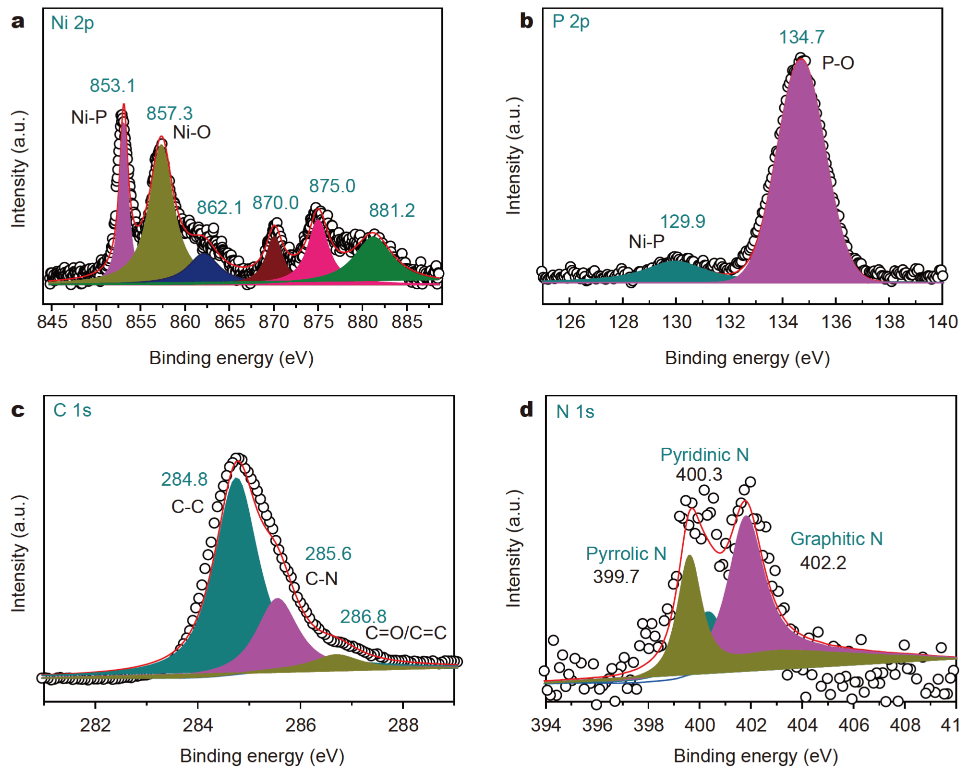

Figure 3 High-resolution XPS spectra of Ni_2P/NC porous spheres: (a) Ni 2p, (b) P 2p, (c) C 1s and (d) N 1s.

pacity of 450.4 mA h g^{-1} is maintained with the capacity retention of 95.3% and the colulombic efficiency near 100%. The lithium-storage properties are superior to other results in the literatures (Table S1).

The superior rate performance was also analyzed with capacitive behavior. Fig. 5a shows the CV curves at different scan rates. Normally, the scan rate (v) and the current (i) abide the following relationship [44,45],

$$i = av^b, \quad (1)$$

$$i = k_1 v + k_2 v^{1/2}, \quad (2)$$

where a and b are empirical parameters. The b-value (0.5) represents the electrochemical reaction is controlled by ionic diffusion, whereas the value of 1 describes a main capacitive behaviour [46].

Fig. 5b shows the fitted line, and the b-values of the Ni_2P/NC electrode were calculated to 0.89 and 0.95 for the cathodic and anodic peaks, respectively. It points out that the rapid kinetics originates from the pseudocapacitive contribution. Fig. 5c demonstrates that 70% of the total storage is capacitive contribution for the Ni_2P/NC at 1.0 mV s^{-1}. Fig. 5d summarizes the corresponding ratio of capacitive/diffusive contribution under various scan rates. The pseudo-capacitive contributions increase with the scan rates, suggesting that fast kinetics mainly occur on the capacitive storage, determining a superior rate capability and a longer cycling life. The impedance spectrum of the Ni_2P/NC electrode was investigated at different cycles. All the curves exhibit a semicircle shape and sloped line in the high and middle-low frequency regions, respectively (Fig. 5e). The equivalent circuit model was used to fit the impedance parameters (Table S2). The charge transfer resistance (R_{ct}) increases sharply after 20 cycles, implying a high contact and charge transfer resistance. Thereafter, the R_{ct} drops after 50 cycles. Notably, the R_{ct} decreases from 107.2 to 98.6 Ω after 100 cycles compared with the initial value, indicating the as-prepared Ni_2P/NC anode material maintains a good electronic conductivity during the charging-discharging process. Fig. 5f shows the relationship of Z' *vs.* $\omega^{-1/2}$ calculated by fitting the oblique line. Actually, when compared with the pristine electrode, the electrode slope shows negligible changes after 100 cycles, suggesting that rapid lithium diffusion occurs during cycling in the Ni_2P/NC electrode [47].

To further prove the structural stability of the Ni_2P/NC, XAFS was used to analyze the local structure change during the first cycle. Fig. 6a compares the Ni-K edge X-ray absorption near-edge spectroscopy (XANES) spectra

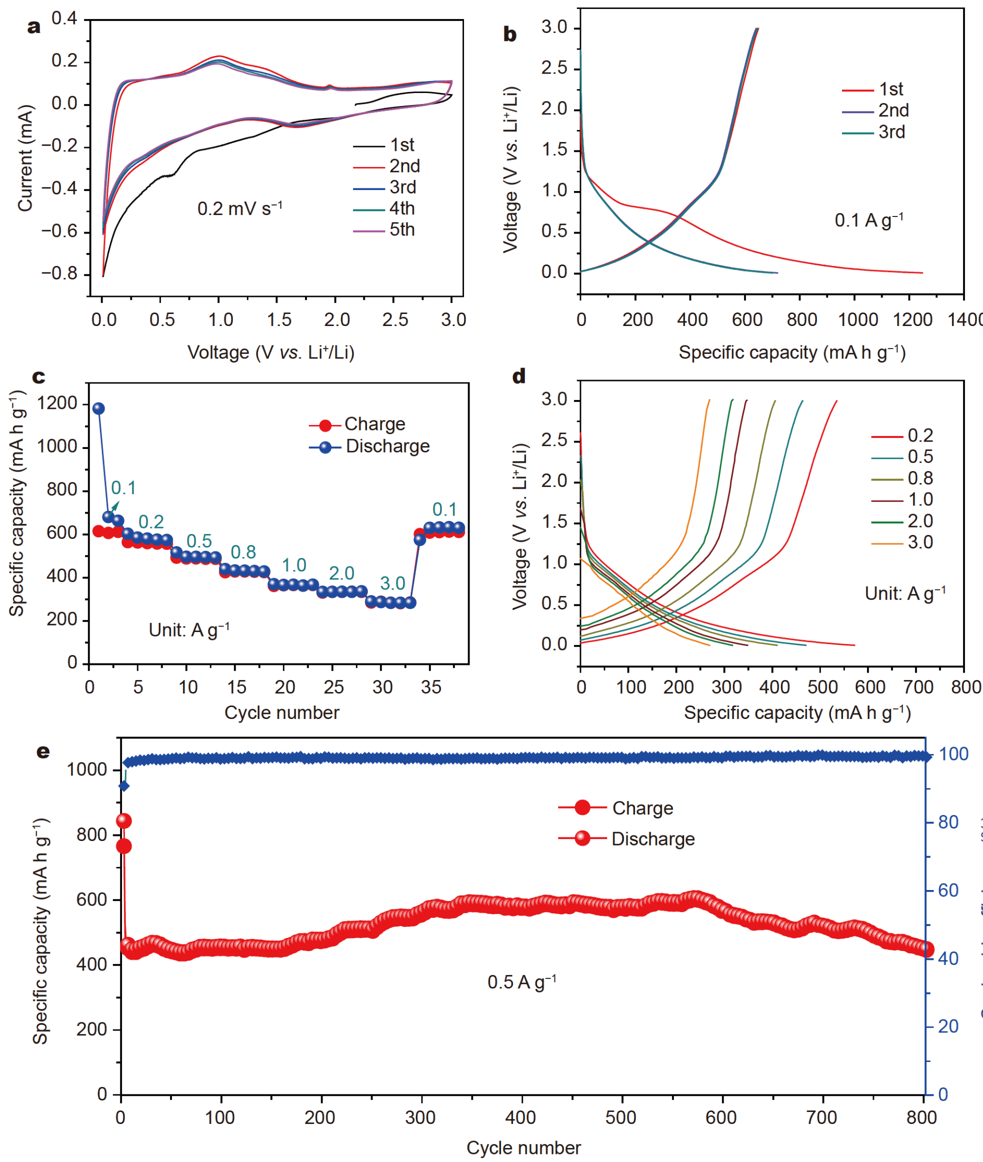

Figure 4 Electrochemical performance of the Ni_2P/NC electrode for lithium-ion batteries: (a) CVs at 0.2 mV s^{-1}; (b) initial charge/discharge curves electrode at 0.1 A g^{-1}; (c, d) rate performance at different current densities; (e) cycling performance at 0.5 A g^{-1} after 800 cycles.

at different discharged and charged states. The Ni absorption edge shifts to lower energy in the fully discharged state close to the energy of the Ni foil, indicating a reduction in the Ni_2P during the lithiation process. The position of Ni-K edge turns back to pristine in the fully charged state and the shape of the Ni-K edge XANES is similar to the pristine spectrum, which is consistent with the formation of Ni_2P after delithiation. The corresponding Fourier-transformed (FT) of the extended X-ray absorption fine structure (EXAFS) curves are shown in Fig. 6b. In these curves, the first peak at ~1.80 Å includes the contributions of the Ni–P and the Ni–Ni bonds. According to the fitting results (parameters in the Table S3), the Ni–P interatomic distance and the coordination numbers slightly decrease when the electrode is discharged to 0.01 V and returns back when charged to 3.0 V. In addition, the wavelet transforms (WT) of Ni-K edge EXAFS oscillations are also provided in Fig. 6c. These contour plots of the Ni_2P/NC present one contribution at ~1.8 Å corresponding to the Ni-P and the Ni-Ni coordination. However, after being charged to 3.0 V, the signal recovers, confirming that the local structure of the Ni_2P/NC is highly reversible in the charge/discharge process. Moreover, the SEM images after 50 and 100

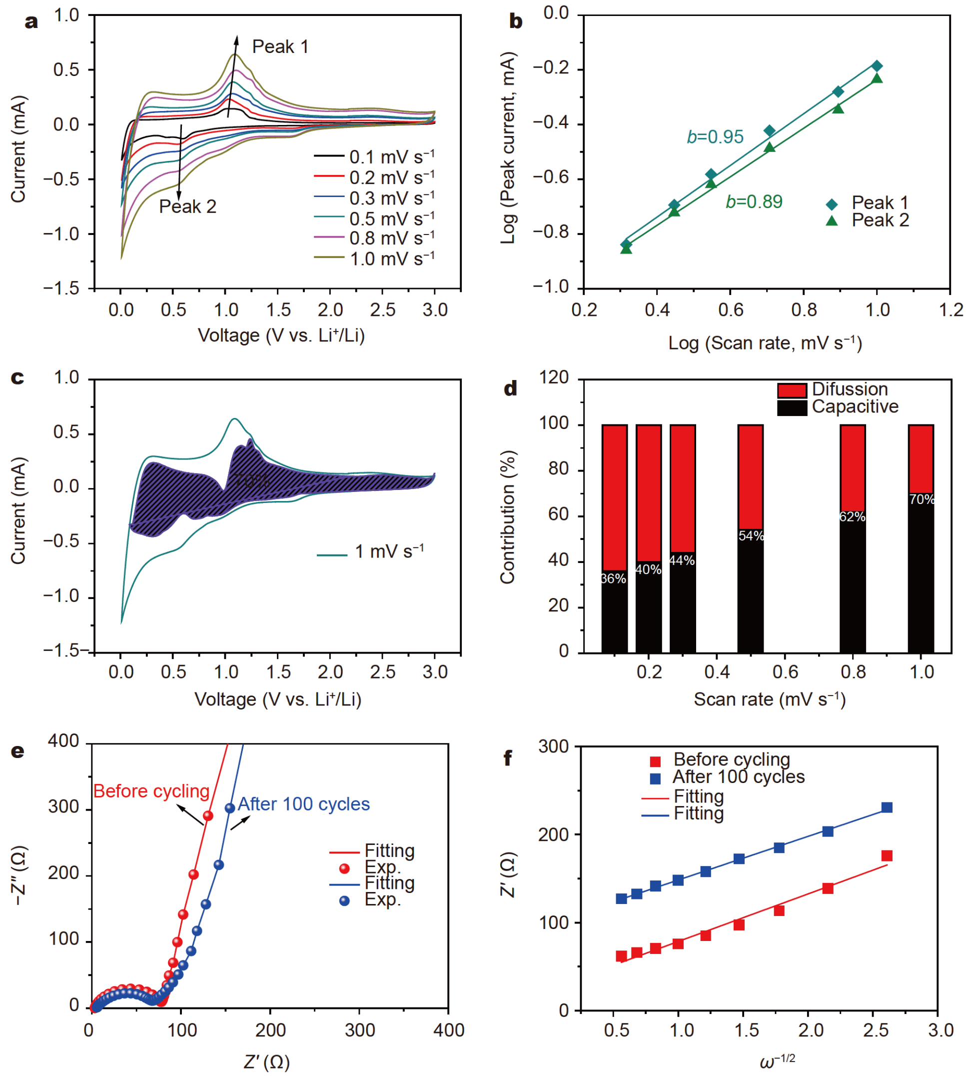

Figure 5 (a) CV curves at different scan rates of the Ni_2P/NC electrode; (b) the relationship between logarithm cathodic and anodic peaks current and logarithm scan rates; (c) the capacitive contribution and diffusion contribution at 1.0 mV s^{-1}; (d) contribution ratio of the capacitive capacities at different scan rates; (e) the Nyquist plots of the Ni_2P/NC electrode at different cycle; (f) the relationship between the real impedance with low frequency for the Ni_2P/NC electrode.

cycles are provided in Fig. S5, it can be seen that the morphology of the Ni_2P/NC spheres is maintained, indicating good structure stability. In order to further confirm the superior electrochemical properties of the Ni_2P/NC, the XPS spectra of the Ni 2p at different stages are compared in Fig. S6. The intensity of the peak (Ni–P) at 853.1 eV decreases while discharging to 0.01 V and recovers at 3.0 V, in agreement with the observed high reversibility of the Ni_2P/NC. The results suggest the high structural stability of the as-prepared Ni_2P/NC porous spheres in the cycling process.

To evaluate a practical application, we assembled full cells by using Ni_2P/NC as the anode and $LiNi_{1/3}Co_{1/3}Mn_{1/3}O_2$ as the cathode. Fig. 7a shows the galvanostatic charge-discharge curves at a current density of 0.1 A g^{-1}, with the charge/discharge capacity in the first cycle of 1020/460 mA h g^{-1}, respectively (based on Ni_2P/NC). The loss of capacity in the first cycle may arise from the irreversible reaction of both anode and cathode [48,49]. Notably, the full cell delivers good rate capability with a reversible specific capacity of 295.6, 235.4 and 187.8 mA h g^{-1} at 0.2, 0.5 and 1.0 A g^{-1}, respectively (Fig. 7b). The reversible capacity of 203.6 mA h g^{-1} can be obtained after 100 cycles at a current density of 0.5 A g^{-1}

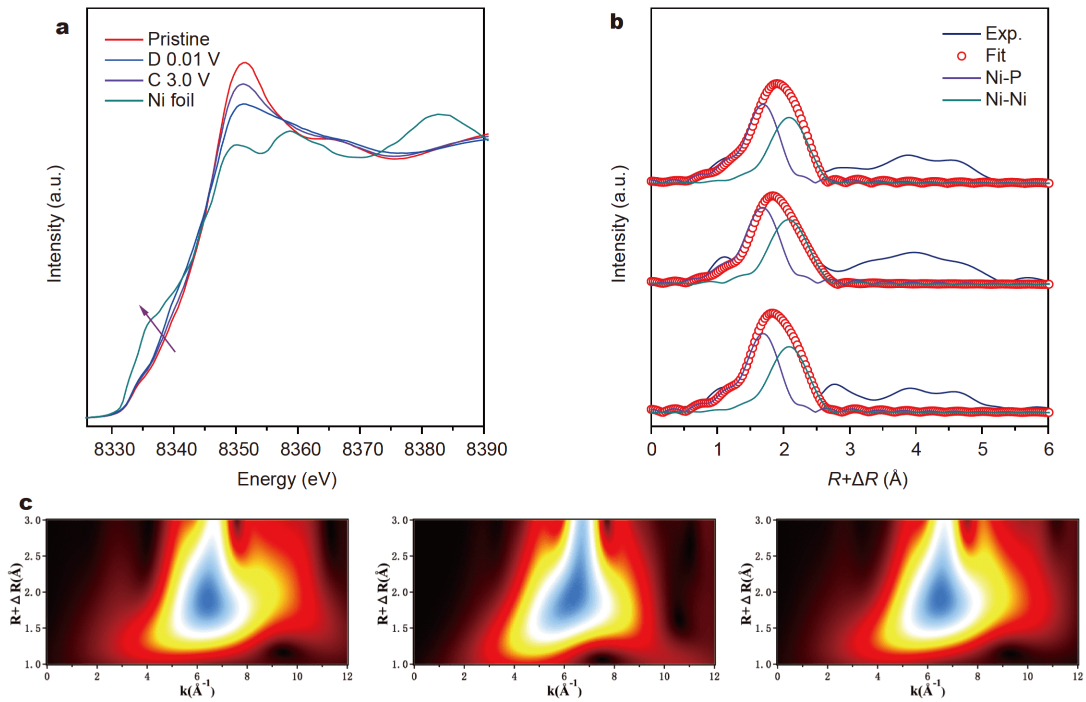

Figure 6 XAFS spectroscopy of the Ni_2P/NC electrode at different charge-discharge states. (a) XANES spectrum; (b) FT of the EXAFS spectra; (c) the corresponding WT-EXAFS images.

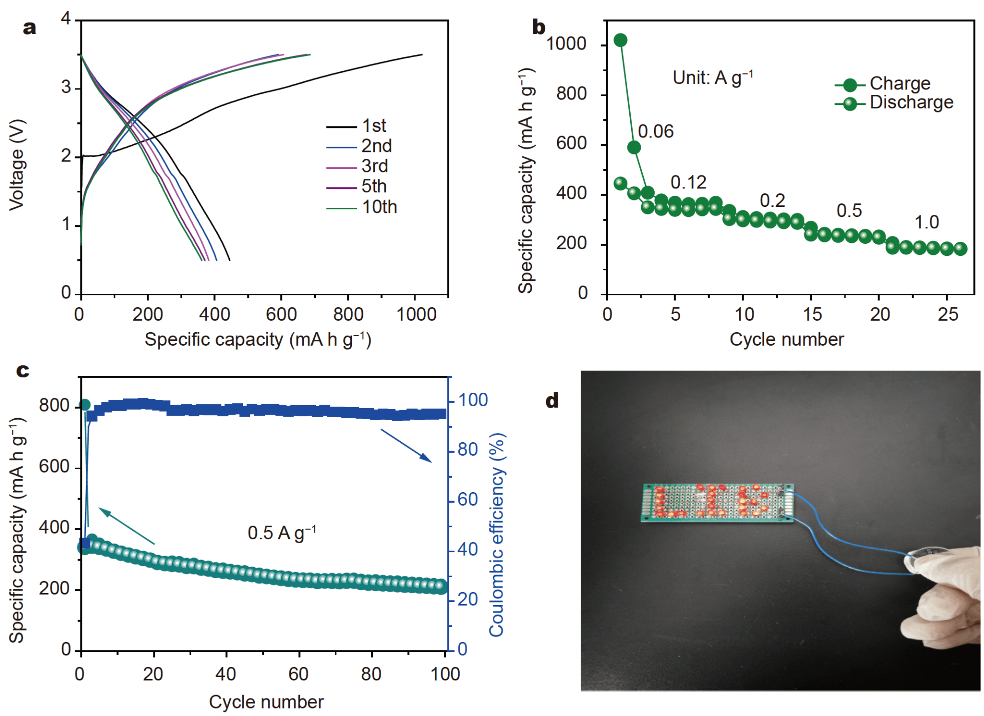

Figure 7 Electrochemical evaluation of the Ni_2P/NC electrode for a full cell: (a) galvanostatic charge/discharge curves at 0.1 A g^{-1} in the voltage range of 0.5–3.5 V; (b) the rate performance at different current densities; (c) cycling performance at the current density of 0.5 mA g^{-1}; (d) image of the full cell that lights LIB logo with 26 LEDs.

with an average coulombic efficiency around 96.8%, indicating the good cyclability of the Ni_2P/NC anode (Fig. 7c). The assembled full cell was applied to power commercial red light-emitting diodes (LEDs). As shown in Fig. 7d, the full cell can easily power the LIB logo with 26 red LEDs. Therefore, we can conclude that the unique nanostructural Ni_2P/NC hybrid composite guarantees its excellent electrochemical performance.

According to the above results, the as-prepared Ni_2P/NC composite exhibits excellent Li-storage performance. This behavior can be associated to: i) the confinement of the small Ni_2P nanoparticles inside the porous carbon matrix. The latter effectively buffers the volume expansion and minimizes aggregation and pulverization of the Ni_2P during the electrochemical process. ii) The unique porous structure that guarantees an excellent contact with the electrolyte and fast Li^+-ion diffusion. iii) The *in situ* MOF-derived carbon enhances the electronic conductivity and provides many active sites.

CONCLUSIONS

In summary, for the first time we employed MOF-Ni spheres as the template to produce the Ni_2P/NC composite containing ultrafine Ni_2P nanoparticles, homogeneously dispersed inside the N-doped carbon matrix. The rational design of this Ni_2P/NC composite exhibits an excellent rate capability (286.4 mA h g^{-1} at 3.0 A g^{-1}) and a remarkable cyclic stability (450.4 mA h g^{-1} after 800 cycles at 0.5 A g^{-1} with the capacity retention of 95.3%). We assign the superior electrochemical performance to the topological structure of this system, which provides the hard structure to the Ni_2P active material and enhances the electronic conductivity during the redox reaction process. We believe that such design and facile strategy will trigger additional attempts to develop the next-generation of Li-based energy storage devices with high performance.

Received 27 January 2020; accepted 2 April 2020; published online 15 May 2020

1 Chu S, Majumdar A. Opportunities and challenges for a sustainable energy future. Nature, 2012, 488: 294–303
2 Chu S, Cui Y, Liu N. The path towards sustainable energy. Nat Mater, 2017, 16: 16–22
3 Mei J, Liao T, Kou L, *et al.* Two-dimensional metal oxide nanomaterials for next-generation rechargeable batteries. Adv Mater, 2017, 29: 1700176
4 Simon P, Gogotsi Y, Dunn B. Where do batteries end and supercapacitors begin? Science, 2014, 343: 1210–1211
5 Yu Z, Tetard L, Zhai L, *et al.* Supercapacitor electrode materials: nanostructures from 0 to 3 dimensions. Energy Environ Sci, 2015, 8: 702–730
6 Pomerantseva E, Bonaccorso F, Feng X, *et al.* Energy storage: The future enabled by nanomaterials. Science, 2019, 366: eaan8285
7 Yu XY, David Lou XW. Mixed metal sulfides for electrochemical energy storage and conversion. Adv Energy Mater, 2018, 8: 1701592
8 Zhao Y, Wang LP, Sougrati MT, *et al.* A review on design strategies for carbon based metal oxides and sulfides nanocomposites for high performance Li and Na ion battery anodes. Adv Energy Mater, 2017, 7: 1601424
9 Liu B, Zhang Q, Jin Z, *et al.* Uniform pomegranate-like nanoclusters organized by ultrafine transition metal oxide@nitrogen-doped carbon subunits with enhanced lithium storage properties. Adv Energy Mater, 2018, 8: 1702347
10 Sun M, Liu H, Qu J, *et al.* Earth-rich transition metal phosphide for energy conversion and storage. Adv Energy Mater, 2016, 6: 1600087
11 Li X, Elshahawy AM, Guan C, *et al.* Metal phosphides and phosphates-based electrodes for electrochemical supercapacitors. Small, 2017, 13: 1701530
12 Chen X, Qiu J, Wang Y, *et al.* Cactus-like iron diphosphide@carbon nanotubes composites as advanced anode materials for lithium-ion batteries. Electrochim Acta, 2018, 259: 321–328
13 Han F, Zhang C, Yang J, *et al.* Well-dispersed and porous FeP@C nanoplates with stable and ultrafast lithium storage performance through conversion reaction mechanism. J Mater Chem A, 2016, 4: 12781–12789
14 Li Q, Ma J, Wang H, *et al.* Interconnected Ni_2P nanorods grown on nickel foam for binder free lithium ion batteries. Electrochim Acta, 2016, 213: 201–206
15 Feng Y, Zhang H, Mu Y, *et al.* Monodisperse sandwich-like coupled quasi-graphene sheets encapsulating Ni_2P nanoparticles for enhanced lithium-ion batteries. Chem Eur J, 2015, 21: 9229–9235
16 Lu Y, Wang X, Mai Y, *et al.* Ni_2P/graphene sheets as anode materials with enhanced electrochemical properties *versus* lithium. J Phys Chem C, 2012, 116: 22217–22225
17 Lu Y, Wang XL, Ge X, *et al.* Graphene-wrapped Ni_2P materials: a 3D porous architecture with improved electrochemical performance. J Solid State Electrochem, 2014, 18: 2245–2253
18 Hou S, Xu X, Wang M, *et al.* Carbon-incorporated Janus-type Ni_2P/Ni hollow spheres for high performance hybrid supercapacitors. J Mater Chem A, 2017, 5: 19054–19061
19 Xie S, Gou J. Facile synthesis of $Ni_2P/Ni_{12}P_5$ composite as long-life electrode material for hybrid supercapacitor. J Alloys Compd, 2017, 713: 10–17
20 Liang H, Xia C, Jiang Q, *et al.* Low temperature synthesis of ternary metal phosphides using plasma for asymmetric supercapacitors. Nano Energy, 2017, 35: 331–340
21 Yuan H, Wu M, Zheng J, *et al.* Empowering metal phosphides anode with catalytic attribute toward superior cyclability for lithium-ion storage. Adv Funct Mater, 2019, 29: 1809051
22 Wang XD, Cao Y, Teng Y, *et al.* Large-area synthesis of a Ni_2P honeycomb electrode for highly efficient water splitting. ACS Appl Mater Interfaces, 2017, 9: 32812–32819
23 Henkes AE, Vasquez Y, Schaak RE. Converting metals into phosphides: A general strategy for the synthesis of metal phosphide nanocrystals. J Am Chem Soc, 2007, 129: 1896–1897
24 Muthuswamy E, Savithra GHL, Brock SL. Synthetic levers enabling independent control of phase, size, and morphology in nickel phosphide nanoparticles. ACS Nano, 2011, 5: 2402–2411

25 Zhang H, Nai J, Yu L, *et al.* Metal-organic-framework-based materials as platforms for renewable energy and environmental applications. Joule, 2017, 1: 77–107
26 Xie Z, Xu W, Cui X, *et al.* Recent progress in metal-organic frameworks and their derived nanostructures for energy and environmental applications. ChemSusChem, 2017, 10: 1645–1663
27 Cao X, Tan C, Sindoro M, *et al.* Hybrid micro-/nano-structures derived from metal–organic frameworks: preparation and applications in energy storage and conversion. Chem Soc Rev, 2017, 46: 2660–2677
28 Cao X, Zheng B, Shi W, *et al.* Reduced graphene oxide-wrapped MoO_3 composites prepared by using metal-organic frameworks as precursor for all-solid-state flexible supercapacitors. Adv Mater, 2015, 27: 4695–4701
29 Wang Q, Zou R, Xia W, *et al.* Facile synthesis of ultrasmall CoS_2 nanoparticles within thin N-doped porous carbon shell for high performance lithium-ion batteries. Small, 2015, 11: 2511–2517
30 Miao X, Yin R, Ge X, *et al.* Ni_2P@carbon core-shell nanoparticle-arched 3D interconnected graphene aerogel architectures as anodes for high-performance sodium-ion batteries. Small, 2017, 13: 1702138
31 Li B, Liu Y, Jin X, *et al.* Designed formation of hybrid nanobox composed of carbon sheathed $CoSe_2$ anchored on nitrogen-doped carbon skeleton as ultrastable anode for sodium-ion batteries. Small, 2019, 15: 1902881
32 Fang Y, Xiao L, Ai X, *et al.* Hierarchical carbon framework wrapped $Na_3V_2(PO_4)_3$ as a superior high-rate and extended lifespan cathode for sodium-ion batteries. Adv Mater, 2015, 27: 5895–5900
33 Wang X, Chen K, Wang G, *et al.* Rational design of three-dimensional graphene encapsulated with hollow FeP@carbon nanocomposite as outstanding anode material for lithium ion and sodium ion batteries. ACS Nano, 2017, 11: 11602–11616
34 Huang L, Cao X, Pan A, *et al.* Bimetallic phosphides embedded in hierarchical P-doped carbon for sodium ion battery and hydrogen evolution reaction applications. Sci China Mater, 2019, 62: 1857–1867
35 Yan L, Dai P, Wang Y, *et al.* *In situ* synthesis strategy for hierarchically porous Ni_2P polyhedrons from MOFs templates with enhanced electrochemical properties for hydrogen evolution. ACS Appl Mater Interfaces, 2017, 9: 11642–11650
36 Tang C, Zhang R, Lu W, *et al.* Energy-saving electrolytic hydrogen generation: Ni_2P nanoarray as a high-performance non-noble-metal electrocatalyst. Angew Chem Int Ed, 2017, 56: 842–846
37 Zhu K, Liu J, Li S, *et al.* Ultrafine cobalt phosphide nanoparticles embedded in nitrogen-doped carbon matrix as a superior anode material for lithium ion batteries. Adv Mater Interfaces, 2017, 4: 1700377
38 Peng S, Li L, Mhaisalkar SG, *et al.* Hollow nanospheres constructed by CoS_2 nanosheets with a nitrogen-doped-carbon coating for energy-storage and photocatalysis. ChemSusChem, 2014, 7: 2212–2220
39 Cheng Y, Li Q, Wang C, *et al.* Large-scale fabrication of core-shell structured C/SnO_2 hollow spheres as anode materials with improved lithium storage performance. Small, 2017, 13: 1701993
40 Wu C, Kopold P, van Aken PA, *et al.* High performance graphene/Ni_2P hybrid anodes for lithium and sodium storage through 3D yolk-shell-like nanostructural design. Adv Mater, 2017, 29: 1604015
41 Lou P, Cui Z, Jia Z, *et al.* Monodispersed carbon-coated cubic NiP_2 nanoparticles anchored on carbon nanotubes as ultra-long-life anodes for reversible lithium storage. ACS Nano, 2017, 11: 3705–3715
42 Li G, Yang H, Li F, *et al.* Facile formation of a nanostructured NiP_2@C material for advanced lithium-ion battery anode using adsorption property of metal–organic framework. J Mater Chem A, 2016, 4: 9593–9599
43 Luo ZZ, Zhang Y, Zhang C, *et al.* Multifunctional 0D-2D Ni_2P nanocrystals-black phosphorus heterostructure. Adv Energy Mater, 2017, 7: 1601285
44 Chao D, Zhu C, Yang P, *et al.* Array of nanosheets render ultrafast and high-capacity Na-ion storage by tunable pseudocapacitance. Nat Commun, 2016, 7: 12122
45 Shen L, Wang Y, Lv H, *et al.* Ultrathin $Ti_2Nb_2O_9$ nanosheets with pseudocapacitive properties as superior anode for sodium-ion batteries. Adv Mater, 2018, 30: 1804378
46 Yang C, Yu S, Lin C, *et al.* $Cr_{0.5}Nb_{24.5}O_{62}$ nanowires with high electronic conductivity for high-rate and long-life lithium-ion storage. ACS Nano, 2017, 11: 4217–4224
47 Zhou D, Fan LZ. Co_2P nanoparticles encapsulated in 3D porous N-doped carbon nanosheet networks as an anode for high-performance sodium-ion batteries. J Mater Chem A, 2018, 6: 2139–2147
48 Li X, Chen G, Le Z, *et al.* Well-dispersed phosphorus nanocrystals within carbon *via* high-energy mechanical milling for high performance lithium storage. Nano Energy, 2019, 59: 464–471
49 Lin X, Wang Y, Chai W, *et al.* Solvothermal alcoholysis synthesis of hierarchically porous TiO_2-carbon tubular composites as high-performance anodes for lithium-ion batteries. Electrochim Acta, 2019, 308: 253–262

Acknowledgements This work was partly supported by the National Natural Science Foundation of China (11705015 and U1832147), the Foundation of Jiangsu Science and Technology Department (BA2016041), the Science and Technology Plan Project of Suzhou (SYG201738 and SZS201710). We sincerely acknowledge Prof. Augusto Marcelli for polishing the language and the staff of the XAS beamlines of Beijing Synchrotron Radiation Facility for their support on this study.

Author contributions Tao S and Cui P engineered the experiments and wrote the paper; Chen S performed the XAFS experiments; Qian B and Song L proposed the experimental design and revised paper; Marcelli A polished the manuscript. All authors contributed to the general discussion.

Conflict of interest The authors declare no conflict of interest.

Supplementary information Supporting data are available in the online version of the paper.

Shi Tao received his PhD degree from the University of Science and Technology of China in 2016. He is currently working as an associate professor in Changshu Institute of Technology. His research focuses on the synthesis of novel electrode materials for application in lithium-ion batteries, sodium-ion batteries and the relationship between structure and property of electrodes using synchrotron radiation technique.

Bin Qian is currently a professor at the School of Electronic and Information Engineering in Changshu Institute of Technology. He received PhD degree from Nanjing University in 2009, Followed by a research stay at Tulane University in USA. His current research interests mainly include the design of novel magnetic materials and energy storage materials for batteries.

Li Song received his PhD in 2006 from the Institute of Physics, Chinese Academy of Sciences (supervised by Prof. Sishen Xie). After four years postdoctoral research at the University of Munich, Germany and Rice University, USA, he became an associate professor at Shinshu University in Japan. He was promoted to professor at the University of Science and Technology of China in 2012. His current research interests are synchrotron radiation study on low dimensional nanostructures and energy-related devices.

金属有机框架衍生Ni_2P嵌入氮掺杂碳多孔微球在锂离子电池中的应用

陶石[1†], 崔培昕[2†], 丛姗[1], 陈双明[3], 吴大军[1], 钱斌[1*], 宋礼[3*], Augusto Marcelli[4]

摘要 过渡金属磷化物(TMPs)/碳复合材料的设计合成在储能领域逐渐引起了研究人员的关注. 本研究以镍基-金属有机骨架材料为模板将磷化镍(Ni_2P)纳米颗粒嵌入到氮掺杂碳 (Ni_2P/NC)多孔微球中. 全面碳封装结构使得Ni_2P纳米颗粒之间的接触更加紧密, 大大提高了结构的完整性和导电性, 使得储锂性能更加优异. 即使在电流密度为3.0 A g^{-1}的情况下, 可逆比容量仍可达286.4 mA h g^{-1}. 在0.5 A g^{-1}电流密度下连续充放电循环800次后, 仍可获得450.4 mA h g^{-1}的可逆比容量. 本研究证实了Ni_2P/NC微观结构的可逆性. 此外, 基于$LiNi_{1/3}Co_{1/3}Mn_{1/3}O_2$||$Ni_2P$/NC的全电池展示了良好的倍率性能和循环寿命. 本研究为寻找应用于储能装置的先进电极材料提供了有力而深入的理论依据.